Advances in Water Resources 000 (2015) 1–13

Contents lists available at ScienceDirect

Advances in Water Resources

journal homepage: www.elsevier.com/locate/advwatres

Particle velocimetry analysis of immiscible two-phase flow in micromodels

Sophie Roman*, Cyprien Soulaine, Moataz Abu AlSaud, Anthony Kovscek, Hamdi Tchelepi

Department of Energy Resources Engineering, Stanford University, Stanford, CA 94305, USA

ARTICLE INFO

Article history:
Available online xxx

Keywords:
Porous media
Multiphase flow
Micromodel
Velocimetry
Pore-scale flow

ABSTRACT

We perform micro-PIV measurements in micromodels using very simple optical equipment combined with efficient image acquisition and processing. The pore-scale velocity distributions are obtained for single-phase flow in porous media with a typical pore size of 5–40 μm at a resolution of 1.8 μm × 1.8 μm vector grid. Because the application of micro-PIV in micromodels is not standard, extensive effort is invested into validation of the experimental technique. The micro-PIV measurements are in very good agreement with numerical simulations of single-phase flows, for which the modeling is well established once the detailed pore geometry is specified and therefore serves as a reference. The experimental setup is then used with confidence to investigate the dynamics of immiscible two-phase flow in micromodels that represent natural complex porous media (e.g., sandstone). For unstable immiscible two-phase flow experiments, micro-PIV measurements indicate that the flow is highly oscillatory long before the arrival of the invading interface. The dynamics are accompanied with abrupt changes of velocity magnitude and flow direction, and interfacial jumps. Following the passage of the front, dissipative events, such as eddies within the aqueous phase, are observed in the micro-PIV results. These observations of complex interface dynamics at the pore scale motivate further measurement of multiphase fluid movement at the sub-pore scale and requisite modeling.

1. Introduction

Detailed understanding of the underlying physics of immiscible two-phase flow in porous media is of great importance in many areas of applied science and engineering including hydro-geology [62], reservoir engineering [18], and CO_2 sequestration [52]. Interest also extends to manufactured porous materials such as fuel cells [31], nuclear safety devices [59], and distillation columns [63]. For example, a fundamental understanding of the displacement mechanisms of a more viscous fluid by a less viscous fluid is critical to optimal hydrocarbon recovery and subsurface storage of CO_2 [72]. In large-scale subsurface flow processes, the behavior is a strong function of the physical and chemical properties of both the injected and resident fluids (viscosity, interfacial tension, density, solubility) and to the porous medium itself (pore size, permeability distribution, wettability of the solid surface, and so on). The competition between the capillary, gravity and viscous forces can lead to highly unstable flow resulting in fingering. These instabilities are the least understood and least predictable phenomena in porous media physics [13].

Previous studies of unstable two-phase flow at the core-scale [7] have demonstrated that these processes are not described adequately by the standard two-phase extension of Darcy's law [43]. This is not surprising given that this Darcy-based approach relies on very strong assumptions, including scale separation between the local events and the large-scale phenomena as well as that the shear stress exerted at the non-wetting/wetting fluid interface has no impact on the large-scale behavior [71]. More importantly, the standard multiphase approach assumes that the fluid–fluid interface is locally stable at the pore-scale [40]. Observation of immiscible two-phase flows in porous media often includes complex mechanisms that span multiple length and time scales. On the one hand, macroscopic phenomena influence the local velocities; on the other hand, pore-scale interfacial events affect the large-scale patterns considerably. It is well established that the interface between two immiscible fluids is transported by abrupt jumps, the so-called Haines jumps [25]. Over the last several decades, it has been demonstrated that these rapid pore-scale events are essential and that they account for a significant fraction of the energy dissipation in the system [42]. Moreover, it has been shown experimentally [11,41] and numerically [6,23] that these jumps reach velocities that are orders of magnitude larger than the mean injection velocities. It has been suggested that such inertial effects that accompany the jumps, completely dictate the invasion patterns [23], and thus, the emerging large-scale behaviors. The origins

* Corresponding author. Tel.: +1 6507256403.
E-mail address: sroman@stanford.edu (S. Roman).

http://dx.doi.org/10.1016/j.advwatres.2015.08.015
0309-1708/

and consequences of these local interfacial processes on large-scale flow in complex porous media remain largely unexplored.

Despite recent great improvements in computational fluid dynamics (CFD) techniques, it is still challenging to model accurately the dynamics of the interface between two immiscible fluids in the pore space at low capillary numbers. For example, interface capturing techniques, such as the Volume of Fluid [26], or Level Set [65] methods, still suffer from spurious currents introduced during the computation of the curvature of the interface. In capillary driven flows, these 'parasitic' velocities can become more important than the physical interface dynamics and lead to completely unphysical invasion patterns. Some authors have applied filtering techniques to minimize the impact of spurious currents [24,30,49]. As demonstrated by the recent experimental work of Moebius and Or [41] and emphasized here, the interface motion is highly complex and one has to be sure that such filtering techniques do not lead to wrong conclusions about the physics associated with multiphase flow. Another challenging aspect of the numerical modeling of two-phase flow in porous media concerns the representation of the contact-line dynamics at the solid walls. The scales associated with such contact lines are measured in nanometers, which is extremely expensive in CFD simulations. Instead, a cut-off size is usually employed, and the real contact angle formed by the two-phases and the solid is up-scaled to the numerical simulation scale [19]. It has been shown that the velocity of the interface near the contact line depends significantly on the model describing the contact angle [34,64]. Accurate measurements of multiphase flow in complex natural porous media are needed to compare these multiphase pore-scale simulators with reference data.

Experiments in simplified two-dimensional porous media, *i.e.,* micromodels that provide direct observations at the pore level [14] are used to develop a detailed understanding of the flow dynamics in complex pore spaces. In these experiments, a silicon wafer is generally used, in which the image of the pore network is etched to a certain depth and bonded to a glass plate to form the micromodel [51]. Reference experimental studies in micromodels of the displacement mechanisms of one fluid by another were performed by Lenormand et al. [36,37] in rectangular ducts. For drainage displacements, *i.e.* a non-wetting fluid such as oil displacing a wetting fluid such as water, they identified three major flow regimes (viscous fingering, capillary fingering, and stable displacement) according to the capillary number and viscosity ratio [35]. These early works have been extended to micromodels of realistic pore patterns, which are particularly interesting to understand subsurface flow processes. The current micromodels can represent pore throats as narrow as several micrometers. Extrapolation of micromodel results to 3D systems must be performed carefully of course; nevertheless, micromodels are an excellent tool for visualizing fluid movements in complex pore geometries [15].

In order to focus on the dynamics of two-phase flows in micromodels, the Particle Image Velocimetry (PIV) technique is used here to obtain instantaneous velocity measurements. This optical method of flow visualization is based on the detection of tracer particles in the flow field. The motion of the seeded particles is used to calculate the velocity field. This technique allows for quantitative comparisons between experimental and numerical data. In the context of microfluidics, in 1998, Santiago et al. [58] introduced micro-Particle Image Velocimetry (micro-PIV) that uses a microscope, micron-sized particles, and a CCD camera to record high-resolution particle-image fields, where the velocity field is calculated by cross-correlating the acquired images [39]. Micro-PIV systems generally use complex and expensive optical systems, including a laser, tracer fluorescing particles, an epifluorescent microscope, a high-speed camera for observation, and optical filters to block the non-fluorescent light disturbances. A recent study has shown the use of two cameras to image the two-immiscible fluids separately using spectral separation [11].

Problems and difficulties faced by performing micro-PIV measurements are numerous, and they must be dealt with using particular attention. Notably, the micro-particles should follow, but not disturb, the flow field [39]. Moreover, light originating from the channel walls and other disturbances have to be blocked, or removed, in order to collect only the light originating from the tracer particles. Moreover, micro-PIV experiments suffer from low particle image concentration and errors due to Brownian motion [39]. Thus, it is essential to choose carefully all the parameters for a micro-PIV measurement: illumination, seeding, optics, implementation of the PIV algorithms, and so on. It is well known that velocimetry measurements may produce results that are not representative of the actual properties of the flow [53], and that they must be validated before they can be used with confidence. The quality of PIV measurements is closely connected to how it is implemented and the data is processed and analyzed. For the study of flow in complex natural porous media, however, it is difficult to satisfy the "ideal" conditions for the implementation of the technique. For these reasons, validation of our approach is emphasized in this paper. Velocimetry measurements were validated by confirming the parabolic Poiseuille flow profile within a square capillary [21], but there are no convincing validation exercises for the more complex pore geometries and velocity distributions of interest in natural porous formations where there is converging and diverging pore space and networks of pore space with variable connectivity among different pores.

There have been several recent studies related to the micro-PIV technique in porous media [11,12,16,21,60]. Chen [16] reported a vector grid of $12\,\mu m \times 6\,\mu m$ in a high-porosity etched-silicon micromodel, the grains are $40\,\mu m$-diameter cylinders arranged with a spacing of $60\ \mu m$ from center to center. Sen et al. [60] measured the velocity field of single phase flow in a 3D glass bead micromodel for pore sizes ranging from 10 to $50\ \mu m$ with velocity vectors distributed onto a grid of $11\ \mu m \times 11\ \mu m$. Blois et al. [11] investigated two-phase flow in a 2D micromodel made of cylinders of $300\ \mu m$ diameter, and they measured the velocity distribution at the interface of both phases. They were able to obtain a vector grid of $5\,\mu m \times 5\,\mu m$ for pore sizes of 40 to $180\ \mu m$. Notably, these micro-PIV measurements have not been validated by comparing the results with reference data or calculations for the micromodel under study. Moreover, to the best of our knowledge, micro-PIV measurements in more complex geometries such the pore networks or realistic porous media replica have not been published yet.

In this work, we performed micro-PIV measurements in micromodels using simple optical equipment with efficient image acquisition and processing. The experimental setup and the simulation work-flow are described in Section 2. In Section 3, we present the pore-scale velocity distributions obtained in the case of a fully saturated porous medium with a typical pore size of 5–40 μm. Extensive comparisons among experimental and simulated results are presented to establish the accuracy and robustness of the experimental method. In Section 4, we use the experimental setup with confidence to investigate the dynamics of immiscible two-phase flow in porous media.

2. Material and methods

In this section, we introduce our experimental framework and the micro-PIV methodology we developed to measure the local velocity distributions. Then, we present the numerical procedure used to obtain reference solutions in the case of fully saturated micromodels.

2.1. Experimental setup

2.1.1. Micromodel

The experimental apparatus includes 2D etched micromodels connected to a syringe pump and placed under a microscope for

Please cite this article as: S. Roman et al., Particle velocimetry analysis of immiscible two-phase flow in micromodels, Advances in Water Resources (2015), http://dx.doi.org/10.1016/j.advwatres.2015.08.015

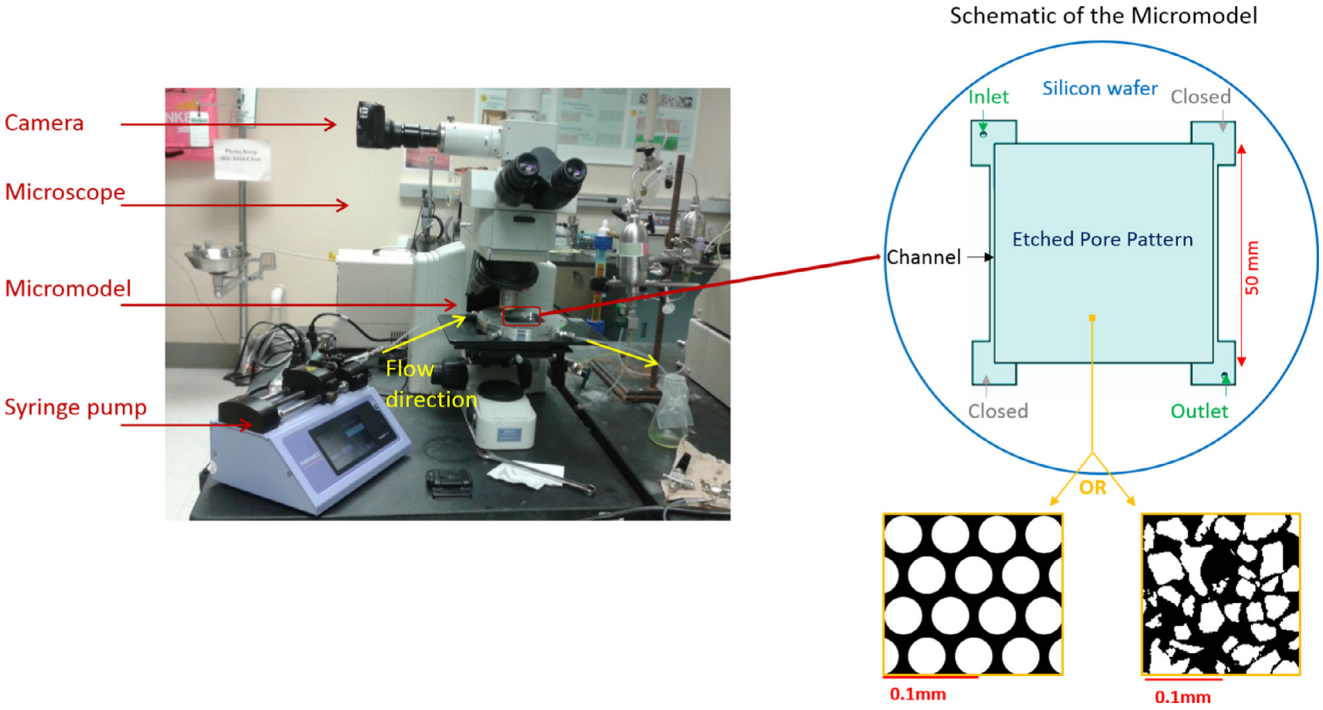

Fig. 1. Experimental setup (left) and schematic of the micromodel (right) with a part a the homogeneous porous pattern (bottom, left) and the sandstone pattern (bottom, right), grains are white and pore space is dark.

flow visualization. The micromodels contain an etched flow pattern that enables the visualization of fluid movement at the pore scale. Two different micromodel patterns are employed: the first represents 40 μm diameter cylindrical grains homogeneously distributed with 10 μm pore throats, and the second consists of a 1:1 realization of pore sizes and pore shapes drawn from a sandstone thin section with grain sizes ranging from 30 to 200 μm and pore throat sizes as narrow as 5 μm (see Fig. 1). The sandstone unit pattern of $1.8\,mm \times 0.6\,mm$ is repeated more than 200 times over the total area of the micromodel. The micromodels contain also two microchannels of 500 μm width along the edges of the porous medium to allow fluids to enter and exit at any point along the side of the porous medium. For both micromodels, the total network dimension is $50\,mm^2$, as shown in Fig. 1. For the homogeneous and sandstone patterns, the porosity is 0.42 and 0.52 respectively.

The micromodel pattern is etched onto silicon using standard photolithography techniques, with an etching depth of 12 μm. Holes are then drilled into the silicon wafer at each corner of the micromodel providing ports for the fluid exit and entry through the fractures. The etched silicon wafer is thoroughly cleaned and then bonded to a glass plate. The silicon is oxidized during bonding, that results in a thin silicon dioxide layer that is water wet. Additional information about the micromodel fabrication process is given by Hornbrook et al. [27] and Buchgraber et al. [14].

The micromodel is mounted in an aluminum holder and the fluid entry/exit ports are aligned to allow fluid delivery and production. A syringe pump (Harvard Apparatus Pump 11 Elite, accuracy ±0.5%) connected to a liquid vessel (Stainless Steel Syringe, Swagelock®) containing water or oil provides a constant injection rate (from 5.10^{-4} to $1.10^{-1}\,mL/min$) into the micromodel. The micromodel is then placed under a Nikon ME600 microscope for flow visualization. Different objective lenses are used either to track the motion of the fluids in the micromodel at a macroscopic scale or to focus on the pore scale. The magnification M and the numerical aperture NA of the objectives lens are: $M = 4$, $M = 10$, 20, 40 and NA = 0.13, 0.3, 0.45, 0.6, respectively. The light source is a Metal Halide lamp, whereas a CCD camera (Nikon Coolpix 5100, 640 × 480 pixels at 30 fps, 8-bits) is used to acquire image sequences. All the experiments are conducted at room temperature and pressure.

2.1.2. Fluids

We conduct different types of experiments. The first consists of a single-phase flow, that is used to validate the micro-PIV measurement methodology by comparison with numerical simulation. The second is a two-phase drainage experiment.

We study single-phase flows through the micromodel for flow rates ranging from 5.10^{-4} to $1.10^{-2}\,mL/min$ and $Re \ll 0.1$ (Reynolds number based on the largest local velocity). In that case, the fluid under study is water seeded with Carboxylate Modified Latex (CML) micro-particles (Polybead Carboxylate Microsphere 1 μm diameter, Polysciences). The density of these particles is close to that of water ($1.05\,g/cm^3$) which minimizes sedimentation. Moreover, CML particles have carboxyl surface functional groups that give the particles hydrophilic surfaces and a negative charge at pH higher than 5. These properties minimize particle aggregation and binding to the walls of the micromodel [3]. The seeding concentration was set at approximately 0.06% by volume.

Thereafter, two-phase displacement experiments are conducted using water mixed with glycerol (65%/35% by weight) as the displaced wetting fluid and n-heptane as the non-wetting displacing fluid. A UV-dye (brilliant yellow water dye, Wildfire) is added to the wetting phase in order to differentiate both phases (3% by weight). The viscosity of the wetting fluid is $\mu_w = 2.7\,cP$ and $\mu_{nw} = 0.417\,cP$ for the non-wetting fluid. A viscosity ratio $M = \mu_{nw}/\mu_w = 0.15$ results. The ratio of density is $\rho_{nw}/\rho_w = 0.6$. The Capillary number is defined as $Ca = \mu_{nw} u/\gamma$. The injection velocity is $u = Q/A$ with A being the cross-sectional area, and Q the imposed flow rate, $Q = 2.5 \times 10^{-3}\,mL/min$. The cross-sectional area is defined as $A = W \times D \times \phi$, with $W = 50\,mm$, $D = 0.010\,mm$ the width and depth of the

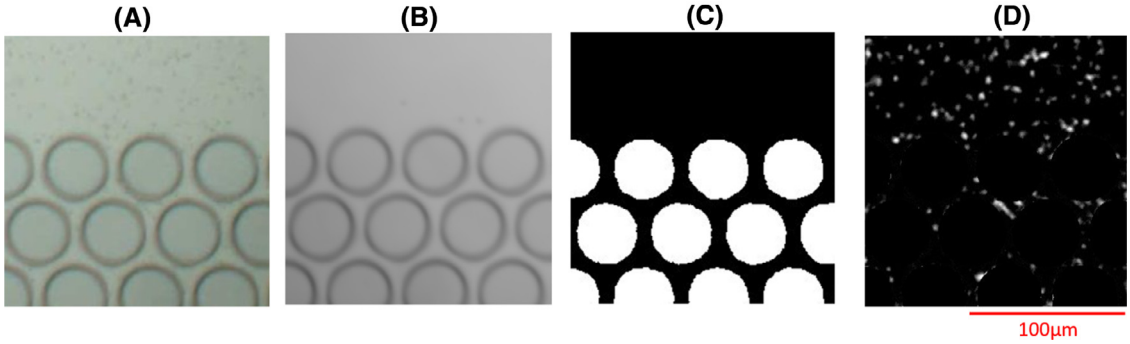

Fig. 2. Homogeneous pattern micromodel: interface between the porous matrix and the fracture. (A) One of the original images acquired with the camera ($\times$ 20 magnification). (B) Reference image of the background after image processing. (C) Binary image of the grains. (D) Image of the particles.

micromodel, respectively, and ϕ the porosity of the micromodel. The interfacial tension γ is in the range 30–50 *dynes*/*cm* for this fluid pair, according to [17]. This leads to $Ca \approx 1 \times 10^{-6}$. This range of parameters is representative of CO_2/brine systems in subsurface aquifer conditions [10,17,44].

2.1.3. Image processing

Sequences of images of particle displacement are recorded using the experimental setup presented above. Compared to standard PIV experiments, we rely neither upon fluorescence from the tracer particles nor on illumination provided by a laser. The raw recorded images (Fig. 2a) are not directly amenable to PIV measurements, due to background noise, low illumination and the presence of the all-important grains. Therefore, effective image pre-processing is required to detect the grains, to remove the background in the pore space and to make the particles bright enough. This pre-treatment allows us to obtain sequences of images that contain only the information regarding particle displacement, see the movies [54] obtained without using any fluorescent particles and optical filters commonly used in standard PIV measurements. This image processing work-flow is performed using MATLAB®'s Image Processing Toolbox. First, each original image (Fig. 2a) of the sequence is converted to grayscale levels. Then, the light intensity fluctuations that may occur over the duration of the sequence are corrected. We also apply a filter using pixel-wise adaptive Wiener filtering [38] to remove the noise. Thereafter, the background image, that corresponds to the average image for the duration of the sequence, is calculated (Fig. 2b). From this background image, the grain edges are detected using binarization and morphological operations [61], see Fig. 2c. This binary image is used to calibrate the experimental images, and to transform spatially the experimental images (rotation, flip), so that they are aligned with the mask images used for the simulations. Then, the background (Fig. 2b) and the grains (Fig. 2c) are subtracted from each image of the sequence, and the final images contain only information related to the moving particles (Fig. 2d). Finally, an intensity histogram filter is applied to highlight in focus particles and remove highly defocused ones [56].

2.1.4. Micro-PIV measurements

Particle Image Velocimetry (PIV) is a technique widely used in hydrodynamics to map the flows in a fluid. PIV results in the accurate quantitative measurement of fluid velocity vectors at a very large number of points simultaneously [1]. The principle of PIV is to record two images of the flow of particles separated by a short time interval. Images are subdivided into many small interrogation windows. The displacements of interrogation windows between the two images are determined through spatial cross-correlation (Fig. 3). Velocity is merely found by dividing the particle displacements by the time between images. Although simple, this operation has to be performed carefully. Indeed, the time interval between two images has to be long enough to enable the displacement between the images of the tracer particles to be determined with sufficient resolution, but short enough to avoid excessive deformation of the pattern formed by particles from one image to the next one. In our case, the time delay ranges from 30 to 120 *ms* according to particle velocities, *i.e.,* according to the imposed flow rate. The delay between images is chosen so that the maximum displacement of particles from one frame to the other is about 3 particle diameters. The process is repeated for all regions in the flow field to obtain the instantaneous velocity distribution [50]. For micro-PIV measurements, the ability of the objective lens of the microscope to focus only on one plane at a time is used. In our case, the thickness over which moving particles are imaged is on the order of the thickness of the micromodel ($\approx 10\,\mu$m). Thus, the micromodel is assumed to be 2-dimensional, and the velocities are measured for only one focal plane that corresponds to the whole thickness.

We perform micro-PIV measurements with PIVlab a MATLAB® tool [67]. This tool allows image pre-processing to improve the measurement quality before the actual image correlation takes place [66], we applied a contrast limited adaptive histogram equalization and an adaptive wiener denoise filter. A direct Fourier transform correlation with multiple passes and deforming windows algorithm is then used for the cross-correlation of the image data. The first pass uses relatively large interrogation windows to calculate the displacement of the image data. The larger the interrogation windows, the better the signal-to-noise ratio, and the more robust is the cross correlation. Large interrogation windows, however, lead to very low vector resolution and to a lack of accuracy in the case of large velocity gradients of particles through the windows. That is why the size of the interrogation windows is reduced in the following iterations. The first coarse correlation pass locally offsets the interrogation window for the subsequent passes. This iterative procedure leads to significantly larger vector resolutions, a high signal-to-noise ratio, and a large dynamic velocity range [66]. We use three passes, starting with a large interrogation window and dividing this size by a factor of two for each subsequent pass. The size of the last (smallest) interrogation window is determined by the spatial resolution of the images, *i.e.* depending on the microscope magnification that is used, such that at least 3 particles are contained within the window, and leading to more than one vector per particle size. For example, when the magnification is $\times$ 40, the spatial resolution of the images is 0.11 μm/pixel which leads to an image particle diameter of 9 pixels. In that case, the smallest interrogation window is 32 $\times$ 32 pixels. For a magnification $\times$ 10, the spatial resolution of the images is 0.4 μm/pixel and the image particle diameter is 2.5 pixels. Then, the smallest interrogation window is decreased to 16 $\times$ 16 pixels. This way, the size of the interrogation window is small enough, so that the particle displacement in the area is uniform, while the interrogation window is large enough so that it contains sufficient information

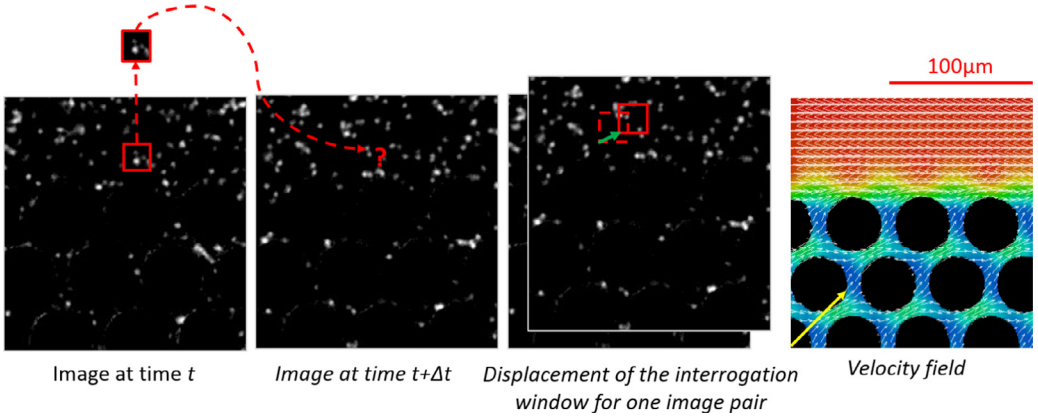

Fig. 3. Principle of the PIV technique.

for the calculation [39]. Finally, the interrogation windows are arranged at 50% overlap [2]. Post-processing of the measurements is performed by filtering outlier data and applying a local median filter [66]. Micro-PIV measurements usually suffer from low particle image density, thus to ensure fully converged measurements, time averaging over at least 50 image pairs is performed in the case of steady flows to increase the number of particle images contributing to a micro-PIV evaluation [39]. This averaging method, however, does not apply for unstable flows, as discussed in Section 3. An example of the velocity vector field obtained, after averaging over 50 PIV realizations, in the homogeneous pattern for a single phase flow at the interface between the fracture and the porous medium is shown in Fig. 3.

2.1.5. Interface tracking

For two-phase experiments, the position of the interface was tracked to determine its velocity during interfacial jumps. For this, the position of the interface is visually detected from one frame to the other, the velocity is determined at the tip of the jumping interface.

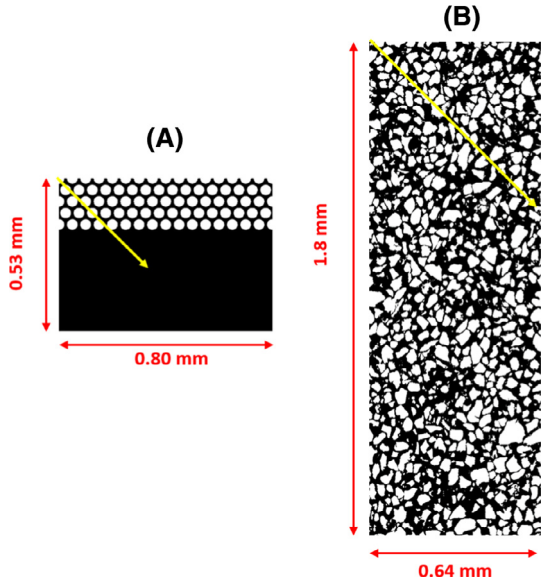

Fig. 4. Geometries and flow directions (yellow arrows) used for the numerical simulations. (A) Homogeneous geometry at the interface fracture-porous medium. (B) Sandstone geometry. (For interpretation of the references to color in this figure legend, the reader is referred to the web version of this article).

2.2. Numerical simulation

To validate the velocity measurements from micro-PIV, we compare in Section 3 the experimental data with 2D numerical simulations of the flow through the different geometries under consideration in the case of fully-saturated micromodels. After this validation stage is performed, we use micro-PIV with confidence to investigate multiphase flow dynamics. For the simulations, we use the computational fluid dynamics toolbox OpenFOAM® [28,68]. To reduce the computational effort of these simulations, we consider representative elementary volumes with periodic boundary conditions instead of the entire micromodels. Fig. 4a depicts the pattern we have used to simulate the flow in the homogeneous micromodel. The top/bottom boundaries and the left/right boundaries are defined as a pair of cyclic conditions, respectively. Fig. 4b illustrates the representative pattern of the sandstone micromodel, for the simulation this pattern has been surrounded by a very thin layer of void space in order to apply cyclic boundary conditions. This surrounding layer is thin enough (less than 3 μm) to have a very low impact on the flow simulation results. Then, each simulation follows the same protocol as described below.

First, the void space is gridded with *snappyHexMesh*, the mesh generation utility provided with OpenFOAM®. This tool grids highly complex geometries with a maximum of hexahedral cells. Due to the numerous narrow throats that appear in complex porous media, in particular for the sandstone sample, the mesh quality is of great importance. As a general rule, these narrow capillary-like pores have to be gridded using at least 10 cells. Mesh convergence analysis has been performed in order to ensure that the simulation results are not affected by the size of the mesh. The final grids of the two different domains contain about 500×10^3 cells (homogeneous pattern) and 14×10^6 cells (sandstone pattern).

Then, the solution of the flow problem is obtained by solving the Stokes equations. The continuity equation for an incompressible fluid reads,

$$\nabla \cdot \mathbf{v} = 0, \tag{1}$$

and the momentum equation in the creeping flow regime with negligible gravitational effects reads,

$$0 = -\nabla \tilde{p} + \mu \nabla^2 \mathbf{v} - \mu \frac{12}{h^2}\mathbf{v} + \frac{\Delta P}{L}\mathbf{e}_0. \tag{2}$$

In these equations, $\mathbf{v}$ stands for the fluid velocity field averaged over the micromodel thickness and $\tilde{p}$ is the deviation to the averaged pressure field over the periodic domain**.** The last term of the right hand side, $\frac{\Delta P}{L}\mathbf{e}_0$, stands for a macroscopic pressure drop per unit length and allows the use of periodic conditions for both $\mathbf{v}$ and $\tilde{p}$ at the inlet and outlet of the computational domain. The vector $\mathbf{e}_0$ determines the average flow field orientation and is set to $\mathbf{e}_0 = \frac{1}{\sqrt{2}}\begin{pmatrix}-1\\1\end{pmatrix}$ in order

to match the experimental conditions. The term $\frac{\Delta P}{L}$ governs the magnitude of the mass flow rate. We chose its value in order to be as close as possible to the experimental data. It is not very important to have an accurate value for $\frac{\Delta P}{L}$, because we are safely in the creeping flow regime, where the streamlines embrace the porous solid structure and are not deformed by the (single-phase) flow. For slow flow, the velocity ratios remain constant regardless of the value of $\frac{\Delta P}{L}$. We base our quantitative analysis on these ratios. The Darcy-like term $\mu \frac{12}{h^2}\mathbf{v}$ is a Hele-Shaw correction [32] to account for the 3D effects of the micromodel, basically we assume a Poiseuille profile in the depth of the micromodel. Consequently, all the simulation results are – in essence – integrated over the micromodel depth. The boundary conditions at the interface between the solid and the fluid are defined as no-slip conditions.

The governing equations (Eqs. (1) and (2)) are discretized using a finite-volume method and solved using the SIMPLE pressure velocity coupling procedure developed by Patankar [46]. We adapted the existing *simpleFoam* solver to integrate the pressure drop source term and the Hele-Shaw correction in the momentum equation.The underrelaxation factors were set to 0.2 for pressure and 0.9 for velocity. The simulations were considered to be fully converged when the residual was below 10^{-9}.

3. Validation of the micro-PIV measurements in micromodels

As discussed in the previous sections, it is important to check the accuracy of the experimental measurements. For that purpose, we conducted single-phase flow experiments and compared measured velocities with numerical simulation for which the numerical models are now well established and serve as reference data. We then discuss the accuracy and robustness of the methodology and its extension to two-phase flow measurements.

3.1. Validation of the micro-PIV measurements in micromodels

In the following, we consider different pore geometries and different magnifications. In order to compare the experimental and numerical results, the velocity magnitude (U_{mag}), the displacement along x axis (U_x) and the displacement along y axis (U_y) are normalized by their maximal value in the area under study, respectively max(U_{mag}), max(U_x) and max(U_y). Note that even though larger domains have been computed, only smaller portions are shown to enhance the visualization.

In Fig. 2 and in supplementary materials [54] we present images and a movie of the particles moving around the grains. We see clearly that there was no agglomeration of particles and frozen images of particles are recorded. Note that, for micro-PIV out of focus particles appear in the recorded images. That is why the particles that are in focus appear as small, well-defined bright dots, whereas the particles that are slightly out of focus are larger and blurred [2].

Prior to comparing micro-PIV results with numerical simulations, we compared them to manual tracking of the particles at different locations in the area under study. This step allowed us to adjust our optimized parameters for the implementation of the PIV and to verify that the measured velocity magnitudes were appropriate. Micro-PIV measurements were also compared successfully to PTV (Particle Tracking Velocimetry) measurements when possible. For further and more accurate validations, only the comparison with numerical simulations are presented in this manuscript.

In Fig. 5, we present the results obtained in the homogenous pattern when looking at the interface between the porous matrix and the fracture. Experimentally, the water is seeded with micro-particles, and flow is imposed across the diagonal of the micromodel at a flow rate of 5.10^{-4} mL/min. The velocity magnitude, the displacement along the x direction, and the displacement along the y are represented for both experiments (Fig. 5, left) and simulation (Fig. 5, right).

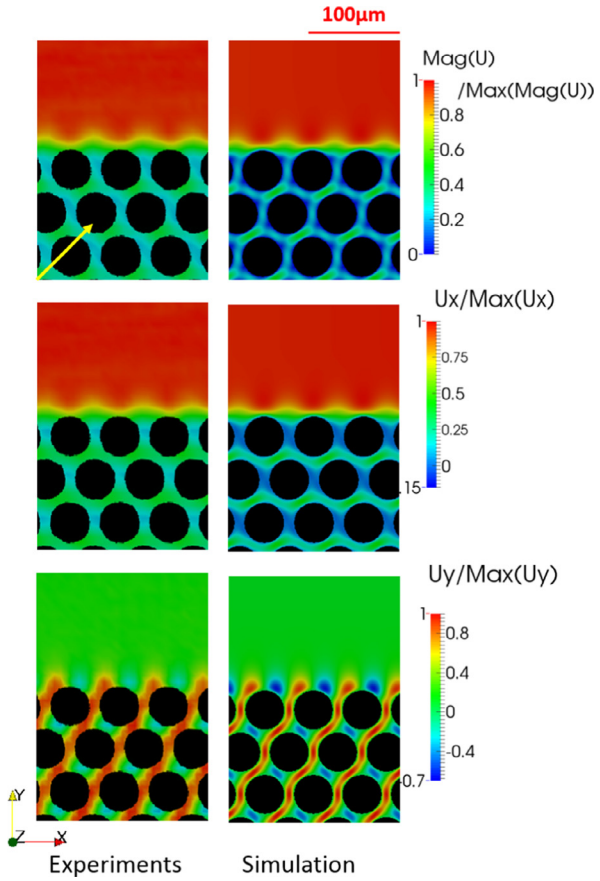

Fig. 5. Single phase flow at the interface porous matrix/fracture. Comparison between micro-PIV measurements and numerical results. The bold arrow reflects the flow direction. Magnification 20×. Experimental vector resolution is 2.2 µm × 2.2 µm.

The flow patterns are in very good agreement between the PIV results and the numerical simulations. Moreover, if we calculate the ratio between the maximal velocity in the fracture and the maximal velocity in the porous media, we find 2.05 experimentally and 1.99 with the simulations, which leads to a 3% relative error in this particular case.

In Figs. 6–8, we present the results obtained in the sandstone pattern. Experimentally, image sequences were recorded at different locations in the micromodel and with different magnifications. The water is still seeded with micro-particles flowing through the micromodel at 45° relative to the normal and an imposed flow rate of 5.10^{-4} mL/min. As previously, we look at the velocity magnitude, the displacement along x and displacement along y, normalized by the maximum value in the area under study. Velocity profiles are also compared. With the lower magnification (10 ×, Fig. 6), the experimental vector resolution is one vector each 3.2 µm, which means a vector grid of 3.2 µ m × 3.2 µ m. We see clearly that the flow patterns are similar in the experiments and the simulations. For a magnification of 20 × (Fig. 7), the resolution is now a 2.2 µm × 2.2 µm vector grid. Finally at 40 × (Fig. 8), for which only a small area of the porous medium is accessible, the vector resolution is one vector each 1.8 µm. The agreement between the experimental and simulation velocity distributions is good, given the difficulty of the micro-dynamics in natural complex porous media. Some differences are explained because of the much greater vector resolution of the simulation results. That is, the simulated velocity distributions are somewhat sharper as compared to the slightly smeared distributions found experimentally. Moreover we found the agreement very good when comparing velocity profiles. Especially, close to the grains and in pore throats, where cluster of particles can be distorted within the interrogation window

Please cite this article as: S. Roman et al., Particle velocimetry analysis of immiscible two-phase flow in micromodels, Advances in Water Resources (2015), http://dx.doi.org/10.1016/j.advwatres.2015.08.015

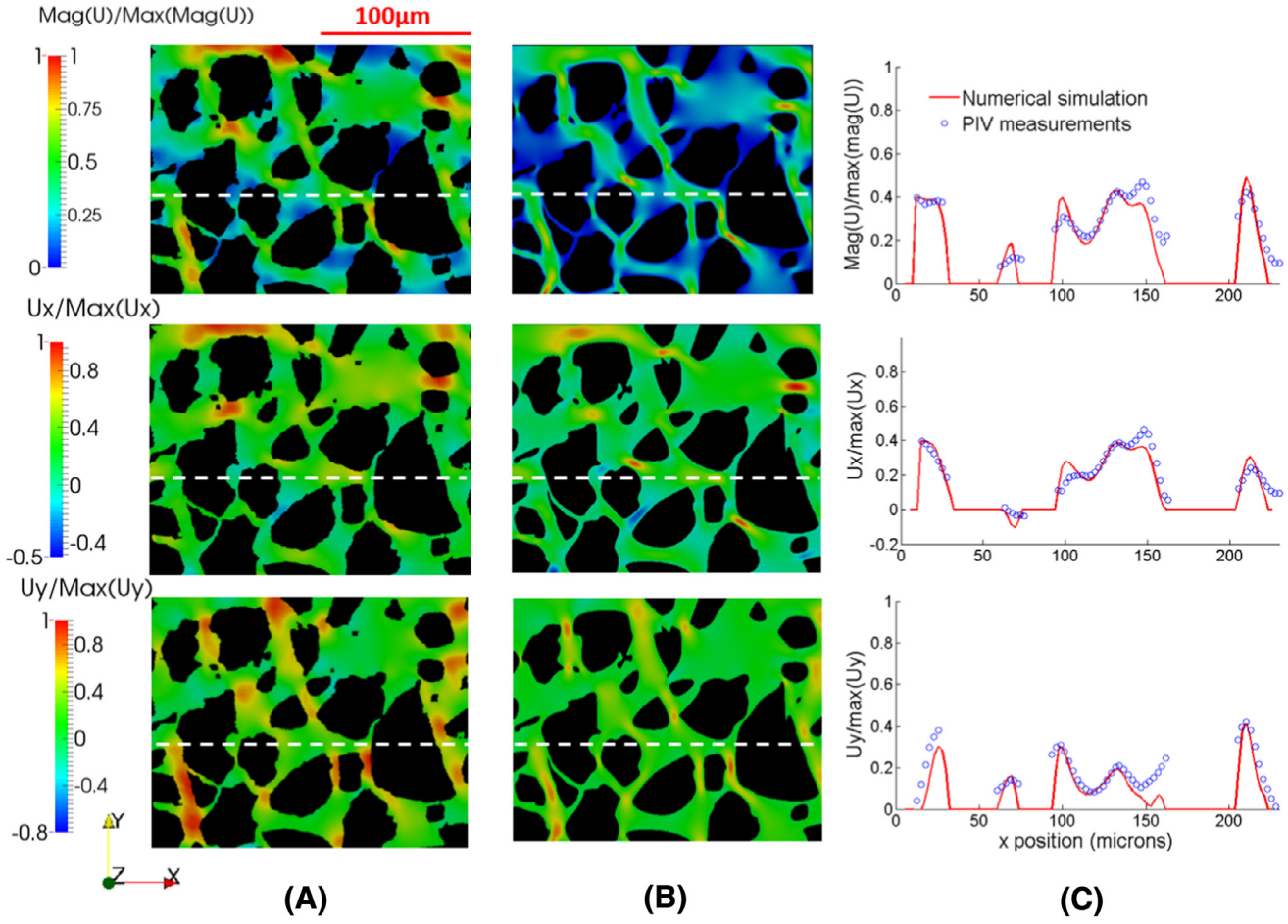

Fig. 6. Single phase flow in sandstone geometry. Comparison of velocity distributions between micro-PIV measurements (A) and numerical results (B). Comparison of velocity profiles plotted along the white dotted line (C). Flow is 45° from top left to bottom right. Magnification 10×. Experimental vector resolution is 3 µm × 3 µm.

for PIV calculation, the agreement is correct (Fig. 6, C). In large pore spaces, the agreement is very good (Fig. 8, C).

3.2. Robustness of the micro-PIV measurements

To ensure high-quality micro-PIV experiments, the parameters for the PIV analysis, the optical system, and the particles have to be chosen carefully [39], otherwise the measured velocities are not representative of the actual velocities of the flow. Here, we discuss these parameters and their implications in our study.

According to the objective and camera properties we used, the size of the image of a particle is 2–8 pixels in diameter. This well satisfies the condition that the particle image should be resolved over at least 2–3 pixels [60]. Another key factor that determines errors in micro-PIV measurements is the choice of the tracing particles [39]. They must be at least two orders of magnitude smaller than the typical pore size. In our case, the smallest pore size is 10 µm, and the particle diameter is 1 µm. Particles need to follow the flow; the response time for the 1 µm particles is calculated to be 6.10^{-2} µs in water and 2.10^{-2} µs in the water/glycerol mixture [39]. These times are significantly smaller than the smallest time-scales in the flow (>1 µs). This ensures that the tracing particles flow with the fluid. Moreover, there might be Brownian motion that limits the minimum particle size in micro-PIV. The error due to Brownian motion relative to the mean displacement is calculated following the guidelines provided by [39]. In this work, the relative error due to Brownian motion reaches a maximum of 5×10^{-4}% in water and 3×10^{-4}% in the mixture water–glycerol [69].

Another concern in PIV measurements is the finite depth of field that results in an underestimation of the midplane velocity, v_{mid}. In fact, in micro-PIV the entire volume of the flow-field is illuminated, resulting in all of the particles in the field of view, *i.e.* in the depth of the micromodel, contributing to the image. Thus, particle tracers away from the central plane also contribute to computing the correlation peak. Adrian [45] introduced the depth-of-correlation, an experimental parameter to estimate the out-of-focus particles that significantly contribute to the correlation function. Our experimental device represents a special case where the depth of correlation is of the same order of magnitude as the depth of our channels and a Poiseuille-type flow profile is expected in the depth of the micromodel. Thus, this entire range of velocities is imaged and all the particles in the depth of the micromodel contribute to the correlation peak. As described previously, to overcome this problem, image pre-processing was performed to highlight the particles that are in focus (*i.e.* at the central plane), and to remove poorly resolved particles. It is well-established that this procedure significantly enhances the quality of the PIV analysis [56,66]. The effect of out-of-focus particles, however, can still lead to an underestimation of the measured velocity [29,57]. The ratio of the measured (v_{mid}^{piv}) to the true velocity at the centerline, $\alpha = v_{mid}^{piv}/v_{mid}$, depends on the channel depth, on the optical system (magnification, numerical aperture, refractive index of the lens immersion liquid) and on the size of the particles [47]. Because the depth of our micromodels is the same everywhere, we expect that this ratio α, predicting the underestimation, remains the same across the whole domain for a given magnification, and is greater than 0.6 [47]. In summary,

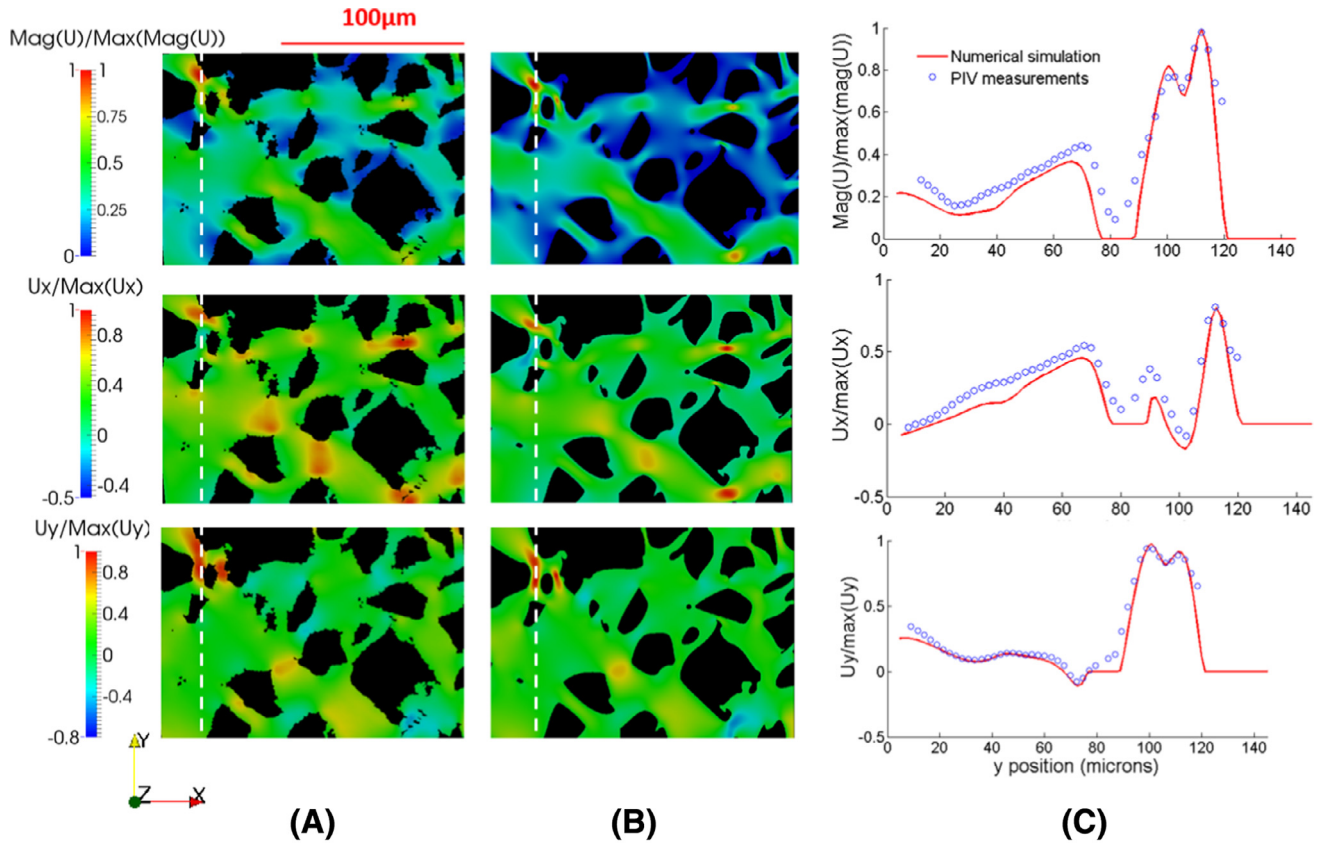

Fig. 7. Single phase flow in sandstone geometry. Comparison of velocity distributions between micro-PIV measurements (A) and numerical results (B). Comparison of velocity profiles plotted along the white dotted line (C). Flow is 45° from top left to bottom right. Magnification 20×. Experimental vector resolution is 2.2 μm × 2.2 μm.

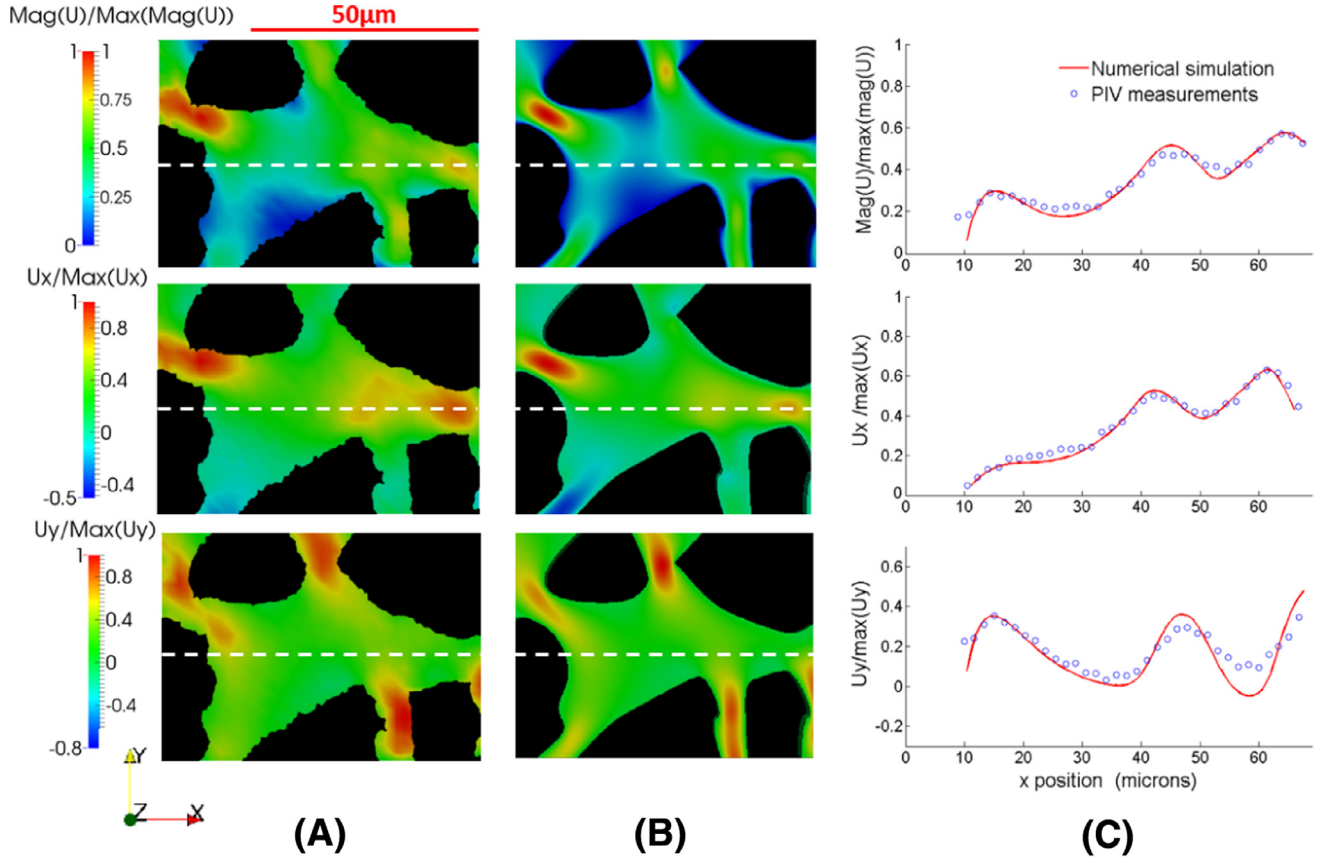

Fig. 8. Single phase flow in sandstone geometry. Comparison of velocity distributions between micro-PIV measurements (A) and numerical results (B). Comparison of velocity profiles plotted along the white dotted line (C). Flow is 45° from top left to bottom right. Magnification 40×. Experimental vector resolution is 1.76 μm × 1.76 μm.

Please cite this article as: S. Roman et al., Particle velocimetry analysis of immiscible two-phase flow in micromodels, Advances in Water Resources (2015), http://dx.doi.org/10.1016/j.advwatres.2015.08.015

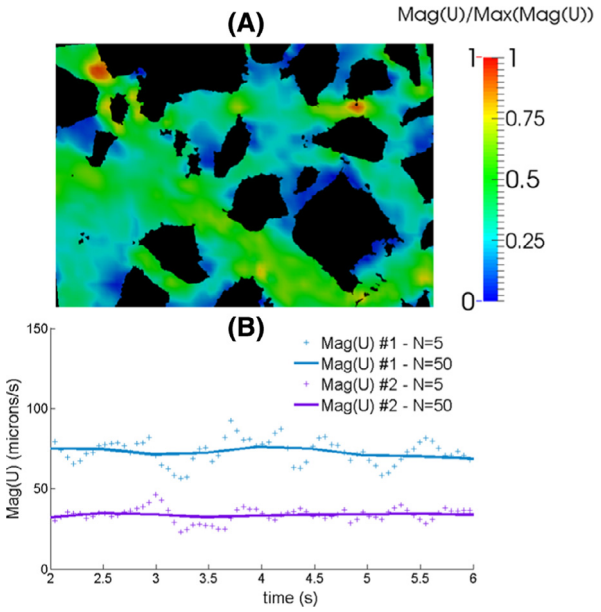

Fig. 9. Micro-PIV measurements in sandstone geometry for a single phase flow. (A) Velocity distribution for 5 image pairs average (same experiment as shown in Fig. 7). (B) Velocity measured by PIV over time at two different positions (#1 and #2) in the micromodel for a single phase flow experiment, for 5 image pair average ($N = 5$) and 50 image pair average ($N = 50$).

experimental data give us αv_{mid}, and for numerical simulation the mean velocity is considered ($= \frac{2}{3} v_{mid}$). As we compared normalized velocity distributions, the difference between 2/3 and α is of no consequence to the results presented. This fact is confirmed by the good agreement between numerical simulations and experimental results.

3.3. Extension to measurements for unstable flows

The micro-PIV measurements are validated and optimized for the single-phase flow case by ensuring high-quality micro-PIV experiments and by comparing the results with numerical simulation. This validation enables us to then investigate two-phase flow mechanisms with confidence with the micro-PIV setup developed. However, there are several questions regarding the extension of micro-PIV measurements from stable to unstable flow. The first concern relates to changes in velocity over time which can take place abruptly. Indeed to obtain the velocity vector field from our sequences of images we used to average over at least 50 image pairs, which is not feasible for unstable flows. Therefore, we performed micro-PIV measurements for a stable single phase flow case, then the results are averaged over 1 to 500 image pairs. Our results (Fig. 9) show that 5 image pairs are enough to represent adequately the actual velocity distribution and magnitude. We present in Fig. 9(A) the velocity distribution for the experiment shown in Fig. 7, if we average over 5 image pairs instead of 50 image pairs (Fig. 7). For a single-phase flow experiment, we also present the velocity magnitude measured by PIV over time at two different positions in the micromodel when averaging over $N = 5$ or $N = 50$ image pairs (Fig. 9, B). Each point at time t represents the average velocity for N PIV realizations, so there is one velocity measurement every N frames. The relative error between averaging over 5 or 50 pairs are equal to 6.5% and 12% for position 1 and 2, respectively. The standard deviation of the velocity over time, that is due essentially to measurement errors and to the accuracy of the syringe pump, is about 4% for both positions for 50 image pair averaging and is about 12% for both positions for 5 image pair averaging. Thus, to average 5 PIV realizations appears reasonable to represent the actual velocity.

Then, in our study of unstable flows, we average over 5 consecutive micro-PIV measurements. In most cases, the time scale corresponding to 5 image pairs is smaller than the time scale of the perturbations of the flow. This procedure ensures that data is not smoothed too much and that changes in velocity over time are represented accurately. The second concern is the changes in velocity magnitude that may occur during unstable two-phase flows. If the particles move too fast, or too slow, from one image to the other, it is difficult to capture their velocity with micro-PIV. Thus, time delay between the image pairs is chosen to ensure a good micro-PIV measurement based on the mean velocity of the flow. If the velocity of the flow decreases over time and becomes very low, we perform a first PIV measurement to measure the larger velocities, then a second measurement is performed to measure accurately the lower velocities, as far as possible, by increasing the time delay between image pairs. Both measurements are then combined. On the contrary when very fast events happen during two-phase displacements (like some Haines jumps), we are not able to measure the velocity with micro-PIV. In fact, the frame rate of the camera is limited to 30 fps, which is not sufficient to capture such rapid events. In that case, we have a lack of velocity measurements for the time step corresponding to the acceleration, that can be resolved by using a high speed video camera. We are able, however, to evaluate the velocity of these events by tracking the interface displacement from one image to the other.

Micro-PIV measurements in micromodels have been validated by comparing experimental and simulation data in the case of single-phase flow. To the best of our knowledge, it is the first time that this kind of measurements are performed in micromodels with pore throat sizes less than 10 μm and with a vector resolution of roughly 2 μm. In addition, micro-PIV measurements are performed using very simple equipment including: a standard camera, an optical microscope, and polymer particles. Thus, these measurements are easily reproducible in any lab. We now investigate two-phase flow mechanisms in micromodels with high accuracy.

4. Investigation of two-phase flow mechanisms using micro-PIV

In this section, we use the micro-PIV technique to investigate two-phase flow mechanisms in complex porous media. Drainage experiments under unfavorable viscosity ratio, *i.e.* mobility ratio that causes flow instabilities, have been conducted for which the density and viscosity ratio between both fluids are representative of CO_2/brine systems under aquifer conditions [17]. The wetting fluid is seeded with micro-particles and a UV-dye is added in order to differentiate both phases. The micromodel is first saturated with the wetting phase. Then, we inject the non-wetting phase at the desired flow rate $2.5.10^{-3}$ mL/min. Once the second phase enters the micromodel, we record movies at different locations and different magnifications in the micromodel by following the interface progression. Because the non-wetting phase is not seeded with micro-particles, we do not image flow patterns within that phase. We measured the velocity fields within the wetting phase and we tracked the interface movements.

4.1. Instabilities of the wetting phase

After the arrival of the oil interface in the micromodel (t_0), the flow is progressively perturbed in the micromodel. Our first observation is that, close to the interface migration areas, the flow organization is dramatically altered compared with the single-phase case. In Fig. 10, we present the velocity distributions for a single phase flow (A) and for the wetting phase during the two-phase experiment (B), at the time of the arrival of the oil interface just upstream of this area (C), 6 min after t_0. The flow directions and intensities are clearly perturbed compared to single-phase flow. Fig. 11 shows the first (A, top) and the last (A, bottom) images of a movie recorded during the drainage. The grains are black, the water phase is green with black

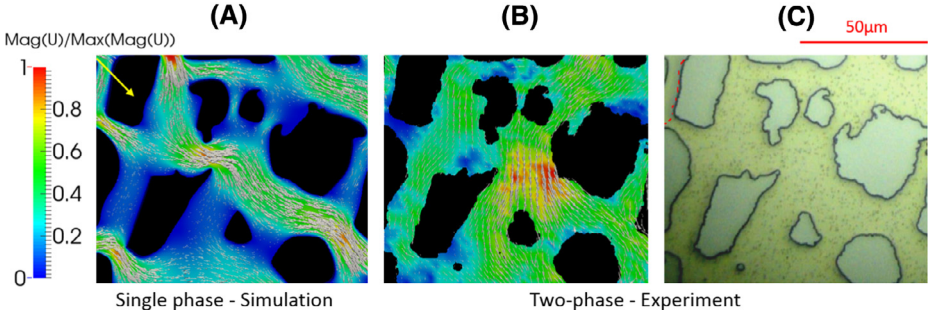

Fig. 10. Velocity magnitude distribution and velocity vectors for a single phase flow case (left) and of the wetting phase during a drainage experiment (middle). Right: image of the flow, grains are gray, water is green with particles, oil is white, the oil interface, highlighted in red, just arrives upstream this porous area. Arrow: flow direction. (For interpretation of the references to color in this figure legend, the reader is referred to the web version of this article).

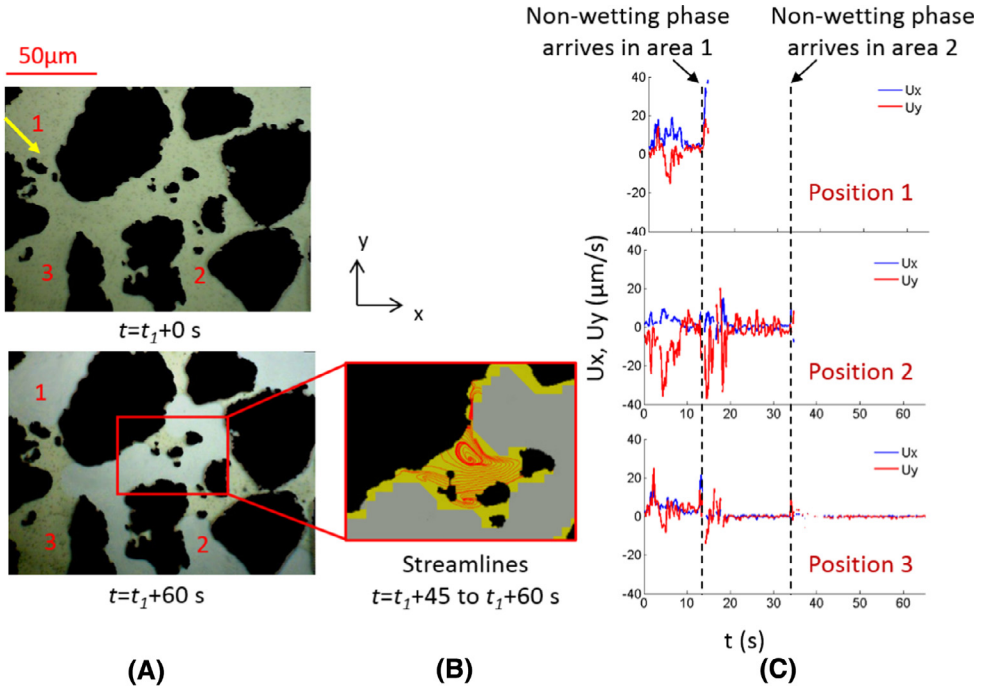

Fig. 11. Two-phase flow experiment. (A) First image $t = t_1 + 0\,s$ (top, arrow: flow direction), last image$t = t_0 + 60\,s$ (bottom) of the sequence, with $t_1 = 10\,min$ the time elapsed between the arrival of the oil interface in the micromodel and the recording of the sequence of images at this location. (B) Plotted streamlines for $t = t_1 + 45 - 60\,s$. (C) Displacement along x (U_x, blue) and y (U_y, red) as a function of time for the positions 1, 2 and 3 depicted in A. (For interpretation of the references to color in this figure legend, the reader is referred to the web version of this article).

particles, and the non-wetting phase appears white. At the beginning of this sequence, 10 min after t_0, the area under study is saturated with water. At this moment, we see clearly that the particles flow back and forth in the pore areas, even before the passage of the interface. The oil-phase enters the area 14 seconds after the start of the recording by the top left corner (point 1, Fig. 11). Twenty seconds later, the oil phase enters the porous area by the bottom edges of the image (point 2, Fig. 11). At the end, we have areas with water (as in point 3, Fig. 11) and areas filled with oil (see movie [54]). In Fig. 11, C we present the displacement along x and y measured by micro-PIV as a function of time for each of these three positions. We see clearly the perturbations of the velocity in the wetting phase. When the non-wetting phase enters the first area, the wetting phase is pushed and we observe its acceleration. After the passage of the interface in this area, because the oil phase is not seeded, we can no longer see particles and so the plotted data stop abruptly for position 1 (Fig. 11, plot data for position 1). Then, large perturbations are recorded at the second location (Fig. 11, position 2). After the passage of the interface, there are still some perturbations and they become smaller, as can be seen at the third location. These back and forth movements only occur at the vicinity of the interface between the fluids, due to the interface migration, they do not occur in the inlet channel of our micromodel and far from the interface. Thus, it is unlikely that this behavior is induced by the syringe pump and we are measuring an effect related to the advancing interface. As reported previously by Blois et al. [11,12], this behavior suggests that pressure instabilities and their propagation further downstream are induced by the Haines jumps that perturb the wetting phase. In fact, the structure of the flow is perturbed before the actual passage of the interface. Moreover, these instabilities continue during the entire passage of the interface, in agreement with Blois et al. [11]. It is likely a consequence of the Haines jumps: for a given time the interface is quasi-static while pushed by the non-wetting phase. Because the pressure in the non-wetting phase keeps increasing due to the injection, the particles move forward slightly. Then, at one point, the pressure locally overpasses the threshold defined by the Young–Laplace law [37] and the non-wetting phase suddenly passes through a throat, invades a pore and we can see the acceleration of the particles in the

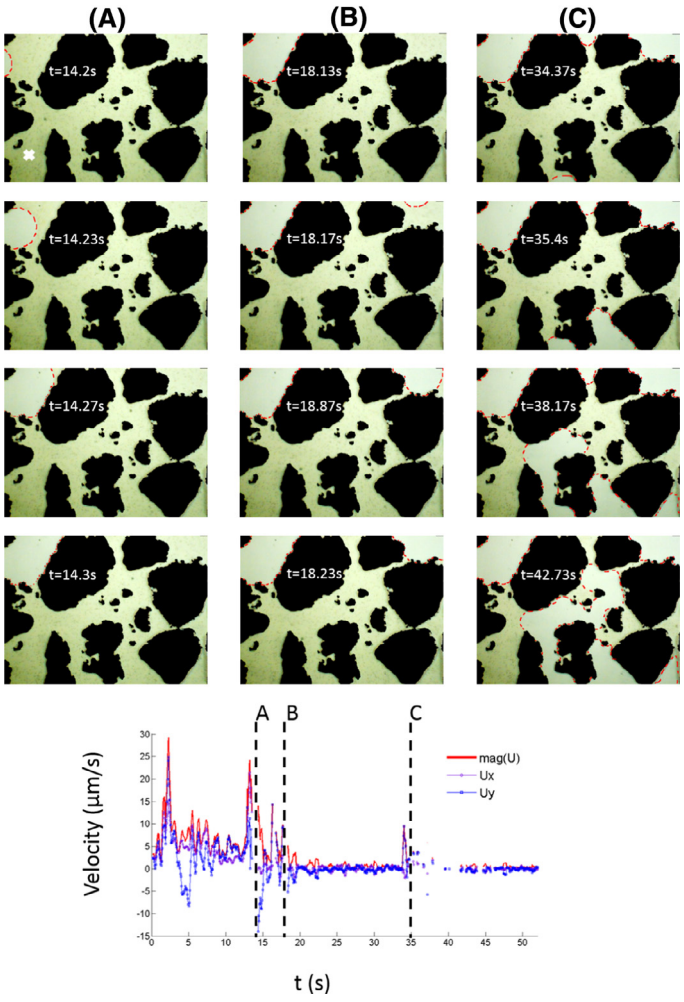

Fig. 12. Two-phase flow experiment: images at different time steps, the interface between both fluids is highlighted in red. Bottom: velocity as a function of time in the water phase measured by micro-PIV, at the location shown by the white cross (first image top left). (For interpretation of the references to color in this figure legend, the reader is referred to the web version of this article).

wetting phase. The pressure is immediately relaxed all along the interface, resulting in a backward movement. This pressure instability may be propagate several pores downstream. This is reminiscent of the theoretical and experimental study of Morrow [42] who showed that during invasion of the pore space, the development of unstable interface configurations cause small oscillations in pressure. These observations suggest that flow perturbations throughout the whole porous medium are driven by local pressure gradients that continuously change in intensity and direction [11]. On the other hand, the paths taken by the non-wetting phase redistribute the flow with the wetting fluid switching direction and magnitude. This also leads to flow instabilities when the wetting phase is pushed into different directions by the surrounding interface. These phenomena emphasize the importance of taking into account local mechanisms related to the drainage pressure and macroscopic effects linked with the topology of the non-wetting fluid [37].

4.2. Interface displacement

We now focus on the interface displacement for the same sequence of images as considered before (Fig. 11). In Fig. 12 we show images of the advancing interface at different time steps, the interface between both fluids is highlighted in red. In this figure we also plotted the velocity measured by micro-PIV as a function of time at the location shown in the first image (white cross). After 14 s of recording in which only water was present in this pore area, the oil interface arrives (Fig. 12A). We estimated the velocity of the jump at 550 μm/s by tracking the position of the tip of the interface at successive time steps during the jump. Then, the interface stays at equilibrium in this pore, stopped by the grain geometry. During this step, the particles in the water phase are still moving with large oscillations in velocity. After 4 s (18 s of recording), the interface arrives in the second location, as shown in Fig. 12B at a velocity of approximately 505 μm/s. The interface remains at equilibrium position in that area for more than 10 seconds and finally enters another pore of the area (Fig. 12C) at a velocity of 130μm/s that decreases to 75μm/s as the interface reaches its final position (last frame in C). The first interface entries in this pore area are really fast and sudden. They are preceded and followed by significant perturbations of the velocity in the wetting phase. Then, the porous domain is filled with oil and water, the water moves very slowly and the oil interface enters the area much more gradually than previously, in fact it encounters more resistance to the flow. The mean velocity of the water phase, far from the arriving interface is around 20–100 μm/s that leads to a local Reynolds number (based on the pore throat characteristic length) *Re* in the order 10^{-5}–10^{-4}. During the passage of the interface *Re* can be as high as 2×10^{-2}, *i.e.* 2–3 order of magnitude greater but still in the Stokes regime.

As stated by Moebius and Or [41] such fast jumps have been known for more than 80 years [25,42]. Recently, some authors have focused on the study of the dynamics of these interfacial jumps [5,41]. Clearly further investigations are needed to describe properly this phenomenon and understand its consequences at the different scales. The micro-PIV setup we have developed offers new possibilities to characterize accurately the complex microdynamics of the jumps.

4.3. Recirculations

As expected for a drainage process, clusters of the wetting phase remain trapped in the asperities of the rock replica after the pores are invaded by the oil. Interestingly, this residual saturation is not immobile, which is contrary to what is commonly accepted; instead, recirculating motion is observed, until the end of the recording, *i.e.*at least 20 s. Fig. 11 shows the streamlines computed from the PIV measurements at the end of the experiment, *i.e.* from $t = 45$ to $t = 60\,s$ for one specific location. Here, the wetting phase is entrapped surrounded by either solid walls, or oil. The grains appear dark, the wetting phase green, and the non-wetting phase is gray. The non-wetting phase and the grains are differentiated from the wetting phase because no velocity is measured by micro-PIV. To our knowledge, these are the first measurements of dissipative recirculations during two phase flow in porous media using this technique. These recirculations are not an isolated phenomenon and have been observed over the entire micromodel.

They are quite similar to lid-driven cavity flow where the shear stress exerted by the flowing oil transmits enough momentum to allow the circular movement of the trapped wetting phase. Basically, the velocity of the fluids interface is equal to the flowing phase (oil). At the same time, the mean velocity of the trapped droplet is equal to zero. As a result, there is a circulation going through the trapped fluid due to the shear stress caused by the momentum transfer from the oil to the trapped glycerin water via the interface. See for instance Beatus et al. [9] for more details about the physics of recirculations in a droplet moving slower than the outer stream.

These observations may have consequences in the modeling of CO_2 sequestration processes. Indeed because we use analog fluids in the parameter range of interest for CO_2 sequestration in deep aquifers, we can expect a similar behavior with supercritical CO_2 and brine. For instance, the pore-to-pore methodology based on micro-CT images of trapped CO_2 combined with numerical simulations

proposed by Andrew et al. [4] to predict the re-mobilization mechanisms of the ganglia might be improved by considering the shear stress at the fluids interfaces. At the field scale, in particular in the presence of a large number of ganglia, these recirculations may have consequences to model the two-phase flow. Indeed, the invading phase may experience an increase of the pressure drop because the shear stress with the trapped wetting phase is a viscous dissipative force. This pressure drop is then a function of the viscosity ratio and of the fluid–fluid momentum exchange area [20,55]. In such case, the viscous dissipative forces should be explicitly included in the multiphase extension of Darcy's law [8,22,33,48,70] and not disregarded contrary to what is usually accepted as discussed by Zarcone and Lenormand [71] and Dullien [22]. These recirculating phenomena may also have implications for multicomponent mass transport by enhancing mixing, or accelerating surface reactions such as dissolution mechanisms.

This work has emphasized that such dissipative mechanisms could not have been observed without particles in the wetting phase. Additional experiments are needed to shed more light on the consequences of these phenomena at the different scales. We hope to clarify the flow patterns in both phases by extending the micro-PIV technique to the two phases simultaneously.

5. Conclusion

We developed and thoroughly validated a micro-PIV system that allows for a better understanding and characterization of the microdynamics of complex flows. The detailed temporal and spatial distributions of the pore-scale velocity field are obtained using simple equipment compared with conventional micro-PIV systems. Thus, these measurements are easily reproducible in any lab. Micro-PIV measurements are performed in micromodels with pore throat sizes less than 10 microns and with a vector resolution of roughly 1μm, for the first time. The experimental measurements are in very good agreement with numerical simulations of steady single-phase flow for which the numerical models are well established. Thereafter, micro-PIV is used with confidence to investigate immiscible two-phase flow properties in porous media with high accuracy.

Our first efforts show that we are able to analyze the velocities for unstable immiscible two-phase flows. The micro-PIV measurements during a drainage experiment have already shown unusual behaviors. In particular, for an unfavorable mobility ratio we find that the flow patterns are highly perturbed compared to single-phase flow. Moreover, the flow patterns within the wetting displaced fluid are perturbed before the actual passage of the interface by local and macroscopic effects. In addition, for the first time we were able to quantify the velocity of dissipative recirculations during two-phase flow. These results are potentially important for accurate numerical representation of processes such as CO_2 injection into saline aquifers and mixing of CO_2 with the resident brine. The observation of these dissipative events opens new lines of research and deserves further experiments and modeling to understand fully their behavior and to characterize their consequences at the different scales.

With this experimental device, we can now provide reliable data to validate numerical two-phase flow simulations that are still in development.

Acknowledgments

S. Roman acknowledges the Petroleum Institute of Abu Dhabi for funding this research. C. Soulaine gratefully acknowledges the support of the Office of Basic Energy Sciences Energy Frontier Research Center under Contract number DE-AC02-05CH11231. It is a pleasure to acknowledge W. Thielicke and E. J. Stamhuis for developing and releasing the PIVlab package, and W. Thielicke for assistance with PIVlab.

Supplementary material

Supplementary material associated with this article can be found, in the online version, at 10.1016/j.advwatres.2015.08.015

References

[1] Adrian RJ. Twenty years of particle image velocimetry. Exp Fluids 2005;39(2):159–69. http://dx.doi.org/10.1007/s00348-005-0991-7.
[2] Adrian RJ, Westerweel J. Particle image velocimetry (cambridge aerospace series). Cambridge University Press; 2011.
[3] Alaskar M, Li K, Horne R. Influence of particle size on its transport in discrete fractures: pore-scale visualization using. 2013.
[4] Andrew M, Bijeljic B, Blunt MJ. Pore-by-pore capillary pressure measurements using x-ray microtomography at reservoir conditions: curvature, snap-off, and remobilization of residual CO_2. Water Resour Res 2014;50(11):8760–74. http://dx.doi.org/10.1002/2014WR015970.
[5] Armstrong RT, Berg S. Interfacial velocities and capillary pressure gradients during haines jumps. Phys Rev E 2013;88:043010. http://dx.doi.org/10.1103/PhysRevE.88.043010.
[6] Armstrong RT, Evseev N, Koroteev D, Berg S. Modeling the velocity field during Haines jumps in porous media. Adv Water Resour 2015;77:57–68. http://dx.doi.org/10.1016/j.advwatres.2015.01.008.
[7] Aryana SA, Kovscek AR. Experiments and analysis of drainage displacement processes relevant to carbon dioxide injection. Phys Rev E 2012;86:1–2. http://dx.doi.org/10.1103/PhysRevE.86.066310.
[8] Baveye P, Sposito G. The operational significance of the continuum hypothesis in the theory of water movement through soils and aquifers. Water Resour Res 1984;20(5):521–30. http://dx.doi.org/10.1029/WR020i005p00521.
[9] Beatus T, Bar-Ziv RH, Tlusty T. The physics of 2D microfluidic droplet ensembles. Phys Rep 2012;516(3):103–45. http://dx.doi.org/10.1016/j.physrep.2012.02.003.
[10] Bennion DB, Bachu S. Dependence on temperature, pressure, and salinity of the IFT and relative permeability displacement characteristics of CO_2 injected in deep saline aquifers. Soc Pet Eng 2006:1–9. http://dx.doi.org/10.2118/102138-MS.
[11] Blois G, Barros J, Christensen K. A microscopic particle image velocimetry method for studying the dynamics of immiscible liquid–liquid interactions in a porous micromodel. Microfluid Nanofluidics 2015;18(5):1391–406. http://dx.doi.org/10.1007/s10404-014-1537-1.
[12] Blois G, Barros JM, Christensen KT. PIV investigation of two-phase flow in a micro-pillar microfluidic device. Delft University of Technology, Faculty of Mechanical, Maritime and Materials Engineering, and Faculty of Aerospace Engineering; 2013.
[13] Buchgraber M. Microvisual investigations to assess and understand enhanced oil recovery processes using etched silicon micromodels. Stanford University; 2013. Ph.D. thesis.
[14] Buchgraber M, Al-Dossary M, Ross C, Kovscek A. Creation of a dual-porosity micromodel for pore-level visualization of multiphase flow. J Pet Sci Eng 2012;86-87:27–38.
[15] Buchgraber M, Clemens T, Castanier LM, Kovscek A. A microvisual study of the displacement of viscous oil by polymer solutions. SPE Reserv Eval Eng 2011;14:269–80. http://dx.doi.org/10.2118/122400-PA.
[16] Chen Q. Microscopic investigation of fluid flow through high porosity porous media and in-situ combustion with aqueous metallic additives. Stanford University; 2005. Master's thesis.
[17] Cinar Y, Riaz A, Tchelepi HA. Experimental study of CO_2 injection into saline formations. SPE J 2009;14:588–94. http://dx.doi.org/10.2118/110628-PA.
[18] Clemens T, Tsikouris K, Buchgraber M, Castanier L, Kovscek A. Pore-scale evaluation of polymers displacing viscous oil–computational-fluid-dynamics simulation of micromodel experiments. SPE Reserv Eval Eng 2013;16(2):144–54. http://dx.doi.org/10.2118/154169-PA.
[19] Cox RG. The dynamics of the spreading of liquids on a solid surface. Part 1: viscous flow. J Fluid Mech 1986;168:169–94. http://dx.doi.org/10.1017/S0022112086000332.
[20] Danis M, Quintard M. Modélisation d'un écoulement diphasique dans une succession de pores. Oil Gas Sci Technol 1984;39(1):37–46. http://dx.doi.org/10.2516/ogst:1984003.
[21] Datta SS, Chiang H, Ramakrishnan TS, Weitz DA. Spatial fluctuations of fluid velocities in flow through a three-dimensional porous medium. Phys Rev Lett 2013;111:064501. http://dx.doi.org/10.1103/PhysRevLett.111.064501.
[22] Dullien F. 5 – multiphase flow of immiscible fluids in porous media. In: Dullien F, editor. Porous media. San Diego: Academic Press; 1992. p. 333–485.
[23] Ferrari A, Lunati I. Inertial effects during irreversible meniscus reconfiguration in angular pores. Adv Water Resour 2014;74:1–13. http://dx.doi.org/10.1016/j.advwatres.2014.07.009.
[24] Francois MM, Cummins SJ, Dendy ED, Kothe DB, Sicilian JM, Williams MW. A balanced-force algorithm for continuous and sharp interfacial surface tension models within a volume tracking framework. J Comput Phys 2006;213(1):141–73.
[25] Haines WB. Studies in the physical properties of soil. V. The hysteresis effect in capillary properties, and the modes of moisture distribution associated therewith. J Agric Sci 1930;20:97–116. http://dx.doi.org/10.1017/S002185960008864X.
[26] Hirt CW, Nichols BD. Volume of fluid VOF method for the dynamics of free boundaries. J Comput Phys 1981;39:201–25. http://dx.doi.org/10.1016/0021-9991(81)90145-5.

[27] Hornbrook J, Castanier L, Pettit P. Observation of foam/oil interactions in a new, high-resolution micromodel. Society of Petroleum Engineers; 1991. http://dx.doi.org/10.2118/22631-MS.
[28] Jasak H. Error analysis and estimation for the finite volume method with applications to fluid flows. Department of Mechanical Engineering Imperial College of Science, Technology and Medicine; 1996. Ph.D. thesis.
[29] Kloosterman A, Poelma C, Westerweel J. Flow rate estimation in large depth-of-field micro-piv. Exp Fluids 2011;50(6):1587–99. http://dx.doi.org/10.1007/s00348-010-1015-9.
[30] Lafaurie B, Nardone C, Scardovelli R, Zaleski S, Zanetti G. Modelling merging and fragmentation in multiphase flows with SURFER. J Comput Phys 1994;113(1):134–47. http://dx.doi.org/10.1006/jcph.1994.1123.
[31] LaManna J, Bothe J, V J, Zhang F-Y, Mench M. Measurement of capillary pressure in fuel cell diffusion media, micro-porous layers, catalyst layers, and interfaces. J Power Sources 2014;271:180–6.
[32] Lamb H. Hydrodynamics. 3rd ed. Cambridge University Press; 1906.
[33] Lasseux D, Quintard M, Whitaker S. Determination of permeability tensors for two-phase flow in homogeneous porous media: theory. Transp Porous Media 1996;24:107–37. http://dx.doi.org/10.1007/BF00139841.
[34] Legendre D, Maglio M. Comparison between numerical models for the simulation of moving contact lines. Comput Fluids 2014;1:2–13. http://dx.doi.org/10.1016/j.compfluid.2014.09.018.
[35] Lenormand R, Touboul E, Zarcone C. Numerical models and experiments on immiscible displacements in porous media. J Fluid Mech 1988;189:165–87. http://dx.doi.org/10.1017/S0022112088000953.
[36] Lenormand R, Zarcone C. Role of roughness and edges during imbibition in square capillaries. Soc Pet Eng 1984:1–17. http://dx.doi.org/10.2118/13264-MS.
[37] Lenormand R, Zarcone C, Sarr A. Mechanisms of the displacement of one fluid by another in a network of capillary ducts. J Fluid Mech 1983;135:337–53. http://dx.doi.org/10.1017/S0022112083003110.
[38] Lim J. Two-dimensional signal and image processing. 1990.
[39] Lindken R, Rossi M, Große S, Westerweel J. Micro-particle image velocimetry (μPIV): recent developments, applications, and guidelines. Lab Chip 2009;9(17):2551–67. http://dx.doi.org/10.1039/B906558J.
[40] Méheust Y, Løvoll G, Måløy K, Jørgen K, Schmittbuhl J. Interface scaling in a two-dimensional porous medium under combined viscous, gravity, and capillary effects. Phys Rev E 2002;66:051603. http://dx.doi.org/10.1103/PhysRevE.66.051603.
[41] Moebius F, Or D. Interfacial jumps and pressure bursts during fluid displacement in interacting irregular capillaries. J Colloid Interface Sci 2012;377:406–15. http://dx.doi.org/10.1016/j.jcis.2012.03.070.
[42] Morrow NR. Physics and thermodynamics of capillary action in porous media. Ind Eng Chem 1970;62(6):32–56. http://dx.doi.org/10.1021/ie50726a006.
[43] Muskat M. Physical principles of oil production. New York: McGraw-Hill; 1949.
[44] Nordbotten J, Celia M, Bachu S. Injection and storage of CO_2 in deep saline aquifers: analytical solution for CO_2 plume evolution during injection. Transp Porous Media 2005;58(3):339–60. http://dx.doi.org/10.1007/s11242-004-0670-9.
[45] Olsen MG, Adrian RJ. Out-of-focus effects on particle image visibility and correlation in microscopic particle image velocimetry. Exp Fluids 2000;29(1):S166–74. http://dx.doi.org/10.1007/s003480070018.
[46] Patankar. Numerical heat transfer and fluid flow. Taylor & Francis; 1980.
[47] Poelma C, Kloosterman A, Hierck BP, Westerweel J. Accurate blood flow measurements: Are artificial tracers necessary? PLoS One 2012;7(9):e45247. http://dx.doi.org/10.1371/journal.pone.0045247.
[48] Raats PAC, Klute A. Transport in soils: the balance of momentum. Soil Sci Soc Am J 1968;32(4):452–6. http://dx.doi.org/10.2136/sssaj1968.03615995003200040013x.
[49] Raeini AQ, Blunt MJ, Bijeljic B. Modelling two-phase flow in porous media at the pore scale using the volume-of-fluid method. J Comput Phys 2012;231:5653–68. http://dx.doi.org/10.1016/j.jcp.2012.04.011.
[50] Raffel M, Willert CE, Wereley ST, Kompenhans J. Particle image velocimetry. A practical guide. Springer; 2007.
[51] Rangel-German E, Kovscek A. A micromodel investigation of two-phase matrix-fracture transfer mechanisms. Water Resour Res 2006;42:1–13. http://dx.doi.org/10.1029/2004WR003918.
[52] Riazi M, Sohrabi M, Bernstone C, Jamiolahmady M, Ireland S. Visualisation of mechanisms involved in CO_2 injection and storage in hydrocarbon reservoirs and water-bearing aquifers. Chem Eng Res Des 2011;89(9):1827–40. http://dx.doi.org/10.1016/j.cherd.2011.03.009.
[53] Roman S, Lorthois S, Duru P, Risso F. Velocimetry of red blood cells in microvessels by the dual-slit method: effect of velocity gradients. Microvasc Res 2012;84(3):249–61. http://dx.doi.org/10.1016/j.mvr.2012.08.006.
[54] Roman S, Soulaine C, AlSaud MA, Kovscek A, Tchelepi H. Supplemental material: particle velocimetry analysis of immiscible two-phase flow in micromodels. Adv Water Resour 2015. http://dx.doi.org/10.1016/j.advwatres.2015.08.015.
[55] Rose W. Fluid flow in petroleum reservoirs. II. Effect of fluid–fluid interracial boundary condition. Illinois State Geological Survey; 1960. p. 1–18.Circular 291
[56] Rossi M, Segura R, Cierpka C, Kähler C. On the effect of particle image intensity and image preprocessing on the depth of correlation in micro-PIV. Exp Fluids 2012;52(4):1063–75. http://dx.doi.org/10.1007/s00348-011-1194-z.
[57] Roudet M, Billet A-M, Risso F, Roig V. PIV with volume lighting in a narrow cell: an efficient method to measure large velocity fields of rapidly varying flows. Exp Thermal Fluid Sci 2011;35(6):1030–7.
[58] Santiago J, Wereley S, Meinhart C, Beebe D, Adrian R. A particle image velocimetry system for microfluidics. Exp Fluids 1998;25(4):316–19. http://dx.doi.org/10.1007/s003480050235.
[59] Sapin P, Duru P, Fichot F, Prat M, Quintard M. Pore-scale experimental study of boiling in porous media. In: Proceedings of the 15th international heat transfer conference, IHTC-15. Kyoto, Japan; 2014.
[60] Sen D, Nobes DS, Mitra SK. Optical measurement of pore scale velocity field inside microporous media. Microfluid Nanofluidics 2012;12:189–200. http://dx.doi.org/10.1007/s10404-011-0862-x.
[61] Serra J. Image analysis and mathematical morphology. Orlando, FL, USA: Academic Press, Inc; 1983.
[62] Smirnov NN, Nikitin VF, Maximenko A, Thiercelin M, Legros JC. Instability and mixing flux in frontal displacement of viscous fluids from porous media. Phys Fluids 2005;17(8):1–20. http://dx.doi.org/10.1063/1.1990227.
[63] Soulaine C, Horgue P, Franc J, Quintard M. Gas-liquid flow modeling in columns equipped with structured packing. AIChE J 2014;60(10):3665–74. http://dx.doi.org/10.1002/aic.14550.
[64] Sui Y, Ding H, Spelt PM. Numerical simulations of flows with moving contact lines. Annu Rev Fluid Mech 2014;46(1):97–119. http://dx.doi.org/10.1146/annurev-fluid-010313-141338.
[65] Sussman M, Smereka P, Osher S. A level set approach for computing solutions to incompressible two-phase flow. J Comput Phys 1994;114(1):146–59.
[66] Thielicke W, Stamhuis E. PIVlab – towards user-friendly, affordable and accurate digital particle image velocimetry in matlab. J Open Res Softw 2014;2(1):1–10. http://dx.doi.org/10.5334/jors.bl.
[67] Thielicke W, Stamhuis EJ. PIVlab – time-resolved digital particle image velocimetry tool for MATLAB (version: 1.4) 2014. http://dx.doi.org/10.6084/m9.figshare.1092508.
[68] Weller HG, Tabor G, Jasak H, Fureby C. A tensorial approach to computational continuum mechanics using object-oriented techniques. Comput Phys 1998;12:620–31. http://dx.doi.org/10.1063/1.168744.
[69] Wereley S, Santiago J, Chiu R, Meinhart C, Adrian R. Micro-resolution particle image velocimetry. In: Proceedings of micro- and nanofabricated structures and devices for biomedical environmental applications, 3258; 1998. p. 122–33. http://dx.doi.org/10.1117/12.304370.
[70] Whitaker S. Flow in porous media II: The governing equations for immiscible two-phase flow. Transp Porous Media 1986;1:105–25. http://dx.doi.org/10.1007/BF00714688.
[71] Zarcone C, Lenormand R. Détermination expérimentale de couplage visqueux dans les écoulements diphasiques en milieu poreux. Comptes Rendus Acad Sci Paris Series II 1994;318:1429–35.
[72] Zhang C, Oostrom M, Wietsma TW, Grate JW, Warner MG. Influence of viscous and capillary forces on immiscible fluid displacement: pore-scale experimental study in a water-wet micromodel demonstrating viscous and capillary fingering. Energy Fuels 2011;25:3493–505. http://dx.doi.org/10.1021/ef101732k.